Chemical Engineering Journal 373 (2019) 1144–1157

Contents lists available at ScienceDirect

Chemical Engineering Journal

journal homepage: www.elsevier.com/locate/cej

Assembly of AgI nanoparticles and ultrathin g-C_3N_4 nanosheets codecorated Bi_2WO_6 direct dual Z-scheme photocatalyst: An efficient, sustainable and heterogeneous catalyst with enhanced photocatalytic performance

Wenjing Xue[a,b], Danlian Huang[a,b,*], Jing Li[a,b], Guangming Zeng[a,b,*], Rui Deng[a,b], Yang Yang[a,b], Sha Chen[a,b], Zhihao Li[a,b], Xiaomin Gong[a,b], Bo Li[a,b]

[a] *College of Environmental Science and Engineering, Hunan University, Changsha 410082, PR China*
[b] *Key Laboratory of Environmental Biology and Pollution Control (Hunan University), Ministry of Education, Hunan University, Changsha 410082, PR China*

HIGHLIGHTS

- Novel g-C_3N_4/Bi_2WO_6/AgI photocatalyst was prepared by a hierarchical assembly method.
- Notably enhanced photocatalytic performance was obtained compared with pure Bi_2WO_6.
- Improved visible light absorption, charge separation and redox ability were realized.
- Direct dual Z-scheme system was proposed to understand the charge transfer route.

GRAPHICAL ABSTRACT

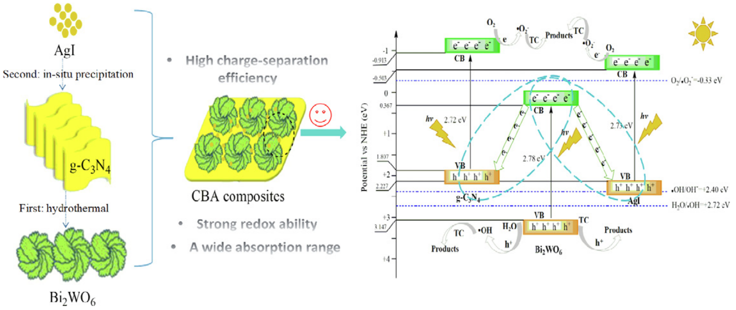

ARTICLE INFO

Keywords:
Photocatalysis
Direct dual Z-scheme
Ternary heterojunction
Antibiotics
g-C_3N_4/Bi_2WO_6/AgI

ABSTRACT

A novel direct dual Z-scheme g-C_3N_4/Bi_2WO_6/AgI (CBA) ternary heterojunction photocatalyst was fabricated through the hydrothermal reaction and a succedent in-situ precipitation route for the first time. Systematic studies showed that the 20% AgI and 60% g-C_3N_4 co-modified Bi_2WO_6 presented the highest photocatalytic performance, achieving 91.13% removal efficiency of tetracycline within 60 min, which was 10.04 times that of pure Bi_2WO_6. The enhanced photocatalytic performance mainly derived from the co-effects of Bi_2WO_6, g-C_3N_4 and AgI and could be summarized as following: i) The g-C_3N_4 nanosheets could be used as carriers for dispersion of Bi_2WO_6 and AgI nanoparticles, preventing their agglomeration; ii) The addition of g-C_3N_4 and AgI could promote the light absorption, resulting in the strengthened light harvesting ability; iii) The intimate contact of Bi_2WO_6, g-C_3N_4, and AgI favored the separation and transfer of photogenerated carriers. Further analysis demonstrated that the path of photogenerated electrons moved exhibited a direct dual Z-scheme pattern in ternary heterojunction, which not only fulfilled the efficient spatial separation of photogenerated electron-hole pairs but also endowed the composites with strong redox capability, thereby boosting the photodegradation efficiency of CBA composite. This work opens a new strategy to constructing multi-component Z-scheme photocatalytic system for environmental decontamination.

---

[*] Corresponding authors at: College of Environmental Science and Engineering, Hunan University, Changsha 410082, PR China.
E-mail addresses: huangdanlian@hnu.edu.cn (D. Huang), zgming@hnu.edu.cn (G. Zeng).

https://doi.org/10.1016/j.cej.2019.05.069
Received 19 February 2019; Received in revised form 24 April 2019; Accepted 13 May 2019

1. Introduction

In recent years, the frequent detection of various antibiotics from aquatic ecosystem has received great concern [1–4]. Recent studies show that humans and animals produce 54,000 tons of antibiotics in China, of which 53,800 tons enter the environment through manifold wastewater treatment methods [5]. The residual antibiotics in the environment could impose negative impacts on organisms and human health [6,7], pollute the drinking water quality [8] and increase the bacterial resistance [9]. Thus, it is imperative to find an efficient way to eliminate the antibiotics from aquatic environment.

Semiconductor-based photocatalysis technology has attracted considerable attention in environmental remediation due to its green, economy and available traits [10,11]. Among numerous semiconductor photocatalysts, bismuth tungstate (Bi_2WO_6, bandgap: 2.60–2.80 eV) has been highlighted for degradation of pollutants in water because of its nontoxicity, excellent photocatalytic performance and chemical stability [12]. However, the photocatalytic activity of single Bi_2WO_6 is still relatively low, and the main restricting factors are: limited light-absorption range and fast electron-hole pairs recombination. Accordingly, many ways have been taken to boost the photocatalytic performance of Bi_2WO_6, for example doping metals [13], controlling morphologies [14], constructing heterojunctions and so on [15]. Among various methods, construction of Bi_2WO_6-based heterojunctions (usually type-II system) has been proved to be a valid strategy to improve photocatalytic efficiency owing to the advantages in separating photogenerated carriers and increasing light-absorption range. Although the separation ability of photogenerated carriers can be enhanced in traditional Bi_2WO_6-based heterojunction photocatalysts, the reduction and oxidation properties of photogenerated electrons and holes will be declined after charge transfer [16]. Therefore, the traditional heterojunction-type photocatalytic system hardly have either high separation efficiency of charge carriers or outstanding redox ability.

Recently, the artificial Z-scheme heterogeneous photocatalytic systems have raised increasing concerns because of the efficient separation of photogeneraged carriers and the superior redox ability [17,18]. Thus far, various Z-scheme photocatalytic systems were reported, for example, TiO_2-Au-CdS [19], Ag_2CO_3/Ag/AgNCO [20], g-C_3N_4/RGO/WO_3 [21], and (Ru/$SrTiO_3$:Rh)/ ($BiVO_4$)-(Fe^{3+}/Fe^{2+}) [22]. However, the present Z-scheme photocatalytic systems usually contains electron conductor (Au, Ag) or redox ion pair (Fe^{3+}/Fe^{2+}) [19,20,22], bring about high construction cost and poor stability of these catalysts in environmental remediation. Hence, the direct Z-scheme systems without electron conductor and redox pair has become the research hotspot [23,24]. Generally, constructing direct Z-scheme heterojunction photocatalytic system with suitable CB and VB potential is better for improving photogenerated carriers separation efficiency and redox ability [16]. Successful cases, like $CuInS_2$/Bi_2WO_6 [25], g-C_3N_4/Bi_2WO_6 [26], Bi_2WO_6/$BiPO_4$ [27], $Bi_2Fe_4O_9$/Bi_2WO_6 [28], Ag_3PO_4/Bi_2WO_6 [29], MoS_2/Bi_2WO_6 [23], and so on. Nevertheless, the overall photocatalytic efficiency of these binary direct Z-scheme heterojunction is still relatively insufficient for practical applications due to the low utilization of sunlight and the slow charge separation and electron migration. Fortunately, studies have proven that the fabrication of suitable ternary heterojunction was more advantageous to enhance the visible light response capability and carriers separation efficiency compared with binary heterojunction [30]. Therefore, it is highly attractive and anticipated for constructing Bi_2WO_6-based Z-scheme ternary heterojunctions through combing with other photocatalysts.

Two-dimensional (2D) graphitic carbon nitride (g-C_3N_4) nanosheets, as a new type of metal-free polymer photocatalyst, has aroused great attention due to its high thermal and chemical stability, unique layered structure, high specific surface area, nontoxicity [31,32]. Silver iodide (AgI) is another a popular photosensitive material and has been applied in the photocatalysis field because of its strong visible-light absorption property and high catalytic activity [33]. However, single g-C_3N_4 and AgI also still exist some problems similar to pure Bi_2WO_6, such as low light utilization and quantum yield. According to previous literatures, g-C_3N_4/Bi_2WO_6 and Bi_2WO_6/AgI composites have been designed to present much improved photocatalytic performance based on the Z-scheme or heterojunctions mechanism [26,33,34]. Moreover, g-C_3N_4 and AgI, as reduction photocatalysts, all possess high CB potential and strong reduction ability, while Bi_2WO_6, as an oxidation photocatalyst, has low VB potential and strong oxidation ability, which is conducive to form Z-scheme photocatalytic system because of their matching band structure. Combing with those analysis, it might be a good idea to construct a novel Bi_2WO_6-based high-efficiency photocatalyst by co-modification of g-C_3N_4 and AgI.

Herein, a novel g-C_3N_4/Bi_2WO_6/AgI ternary heterojunction was synthesized through a hydrothermal reaction, followed by an in-situ precipitation route. The photocatalytic properties of g-C_3N_4/Bi_2WO_6/AgI composite was studied for the degradation of multiple antibiotics, including tetracycline (TC), ciprofloxacin (CIP), and enrofloxacin (ENR). Photogenerated carriers separation and transfer behavior were evaluated by photocurrent response and electrochemical impedance spectroscopy (EIS). The flat band potential of semiconductor was detected using Mott-Schottky measurements. The generation radical species were measured through trapping experiment and further confirmed by electron spin resonance (ESR) tests. Moreover, a direct dual Z-scheme photodegradation mechanism was affirmed.

2. Experimental section

2.1. Materials and reagents

Bismuth nitrate pentahydrate ($Bi(NO_3)_3{\cdot}5H_2O$), melamine, sodium tungstate ($Na_2WO_4{\cdot}2H_2O$), and potassium iodide (KI) were supplied by Lin en Technology Development Co., Ltd. Silver nitrate ($AgNO_3$), 4-hydroxy-2,2,6,6-tetramethylpiperidine-1-oxyl (TEMPOL), sodium oxalate ($Na_2C_2O_4$), isopropyl alcohol (IPA), TC, CIP, and ENR were purchased from Sinopharm Chemical Reagent Co., Ltd. Ultrapure water (18.25 MΩ·cm) was adopted in whole experiments.

2.2. Synthesis of Bi_2WO_6

Briefly, 0.97 g $Bi(NO_3)_3{\cdot}5H_2O$ was first added to 60 mL of nitric acid (HNO_3, 0.4 M) with ultrasonic for 5 min and magnetic stirring for 8 min, and then followed by dropwise adding 20 mL of 0.05 M $Na_2WO_4{\cdot}2H_2O$ solution with vigorously stirring for 30 min. Subsequently, the mixed suspension was put into a Teflon-lined autoclave with the treatment of heated at 170 °C for 18 h. The obtained sample was filtered out and then washed with ultrapure water followed by ethanol for several times. Finally, the obtained Bi_2WO_6 was dried at 70 °C for 10 h in a vacuum oven.

2.3. Synthesis of g-C_3N_4/Bi_2WO_6 heterojunction

Pure g-C_3N_4 nanosheets were synthesized by a two-step heat-treatment measure according to previous reports [35]. Firstly, 5 g of melamine was put into a ceramic crucible with a cover and then heated at 500 °C for 2 h at a rate of 2 °C/min, and followed by heating at 520 °C for another 2 h at the same heating rate. After cooling to ambient temperature, the obtained product was milled into powder in a mortar and used for the second thermal exploitation treatment. In the second thermal exploitation process, 1 g of the bulk g-C_3N_4 was placed in an open ceramic crucible and heated at 520 °C at a heating rate of 2 °C/min and then kept at this temperature for 4 h. Then, the light-yellow powder of g-C_3N_4 nanosheets were obtained. g-C_3N_4 (60%)/Bi_2WO_6 (labeled as CB) heterojunction was fabricated through the hydrothermal reaction. Briefly, 1.05 g of pure g-C_3N_4 and 0.97 g of $Bi(NO_3)_3{\cdot}5H_2O$ were dispersed to 60 mL of 0.4 M HNO_3 with magnetic stirring for 1 h. The following synthetic steps are the same as that for preparing Bi_2WO_6.

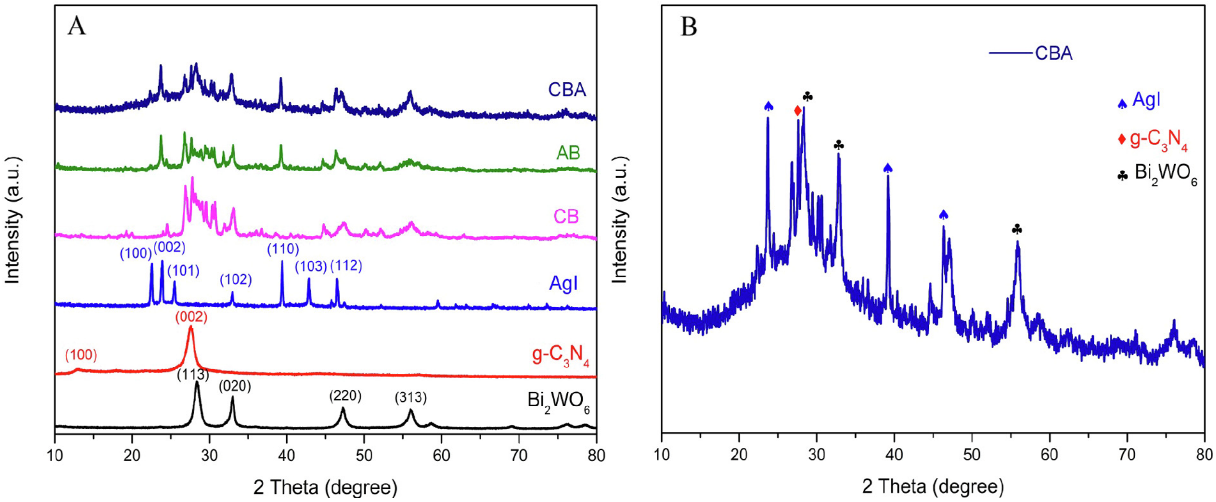

Fig. 1. (A) XRD patterns of the as-prepared samples; (B) The detailed information of the CBA composite.

2.4. Synthesis of g-C_3N_4/Bi_2WO_6/AgI ternary heterojunction

The g-C_3N_4 (60%)/Bi_2WO_6/AgI (20%) (labeled as CBA) composite was obtained by an in-situ precipitation process. Typically, 0.698 g of CB sample was dispersed into 50 mL ultrapure water with ultrasonic for 10 min, and then 0.743 mmol of $AgNO_3$ was added to the aqueous suspension under vigorously stirring for 1 h in the darkness. Subsequently, 25 mL of 0.743 mmol KI was added to the above mixture dropwise at a rate of 1 mL·min^{-1}, followed by vigorously stirring for another 1 h in the darkness. The resultant sample was collected by filtration, washed with ultrapure water and dried at 60 °C for 10 h. For comparison, AgI (20%)/Bi_2WO_6 (labeled as AB) binary heterojunction was synthesized using the identicial method with Bi_2WO_6 instead of CBA. And pristine AgI nanoparticles were also prepared using the identicial procedure without the addition of Bi_2WO_6 and CB sample.

2.5. Characterization

The crystal phase of all samples was measured by powder X-ray diffraction (XRD, Rigaku, Ultima IV). The morphology and crystal lattice parameters of the samples were determined by scanning electron microscopy (SEM, SIGMA HD, Nova450), transmission electron microscopy (TEM, TF20, Joel 2100F) and high-resolution TEM (HRTEM). The elemental composition of CBA composite was tested by energy dispersive spectroscopy (EDS). The X-ray photoelectron spectrum (XPS) of catalysts was measured on a Thermo ESCALAB 250XI spectrometer. The UV–vis diffuse reflectance spectra were performanced on an UV–vis detector (PE lambda 750S). The mineralization ability of samples was detected by shimazu total organic carbon (TOC) analyzer (TOC-VCPH). Three-dimensional excitation-emission matrix fluorescence spectroscopy (3D EEMs) was adopted by a F-4500 spectrofluorimeter. The ESR signals of radicals were analyzed using a JES-FA200 spectrometer under visible light irradiation. The specific surface areas of the samples were measured by Brunauer-Emmett-Teller (BET) based on a N_2 adsorption analyzer (Micromeritics ASAP 2460, USA) and results indicated that the prepared g-C_3N_4 owns a high specific surface area, and after decoration with g-C_3N_4 and AgI, the CBA composite still possesses a relatively large specific surface area. Further details were provided in the Supplementary Material.

2.6. Photoelectrochemical measurement

The photoelectrochemical measurement was performed on a CHI 760E workstation with a conventional three-electrode system. 0.2 M sodium sulfate (Na_2SO_4) was employed as electrolyte. The visible light was supported by a 300 W Xe lamp (CEL-HXF300) with a filter. The Pt plate was adopted act as the counter electrode and an Ag/AgCl electrode was served as the reference electrode. The working electrode was prepared as follows: firstly, 10 mg of the prepared material was dissolved in 200 μL of 25% (W/V) polyvinyl alcohol solution with the treatment of ultrasonic for 2 h; Subsequently, the above mixture was dropped on the surface of a 1 cm × 2 cm fluorine-doped tin oxide (FTO) glass with an effective working area of 1 cm^2 and then dried at 60 °C for 5 h. The photocurrent response was determined by 20 s on–off light. The EIS was measured on a frequency range from 10^5 to 10^{-2} Hz with a 5 mV amplitude. The Mott-Schottky measurements were obtained at the frequency of 1 KHz.

2.7. Photocatalytic activity measurement

The photocatalytic performance of synthesized catalysts was conducted through degrading TC, CIP, and ENR in aqueous solution. The source of visible light was supported by a 300 W Xenon lamp (PLS-SXE300, Perfect Light, Beijing) armed with a 420 nm cut filter. In the experiment, 30 mg of as-prepared catalyst was dispersed in TC (20 mg/L), CIP (10 mg/L), and ENR (10 mg/L) aqueous solution (50 mL), respectively. Before the experiment, the mixed suspension above was firstly stirred in darkness maintained 30 min to reach absorption–desorption equilibrium. Then, 4 mL of sample solution was taken out and filtered at 10 min reaction intervals. The residual concentration of TC, CIP, and ENR was determined at 357 nm, 277 nm, and 271 nm by the UV–vis spectrophotometer, respectively.

3. Results and discussion

3.1. Characterizations

The XRD patterns of Bi_2WO_6, g-C_3N_4, AgI, binary and ternary composites were depicted in Fig. 1. Four distinct diffraction peaks of Bi_2WO_6 at $2\theta = 28.42°$, $33.01°$, $47.21°$ and $55.86°$ correspond to the (1 1 3), (0 2 0), (2 2 0), and (3 1 3) crystal planes of orthorhombic of Bi_2WO_6 (JCPDS 73–1126) [36]. The XRD spectra of g-C_3N_4 shows two peaks at $2\theta = 13.10°$ and $27.31°$ belonged to the (1 0 0) and (0 0 2) planes of graphite-like structure of g-C_3N_4 [37], which were corresponding to the in-planar structural packing motif and the interlayer stacking of the aromatic system, respectively. The peaks of AgI at $2\theta = 22.32°$, $23.71°$, $25.35°$, $32.77°$, $39.20°$, $42.63°$ and $46.31°$ related to (1 0 0), (0 0 2), (1 0 1), (1 0 2), (1 1 0), (1 0 3), and (1 1 2) planes of hexagonal AgI (JCPDS 09–0374) [38]. For two binary and ternary composites, the diffraction peaks belonging to Bi_2WO_6, g-C_3N_4, or AgI

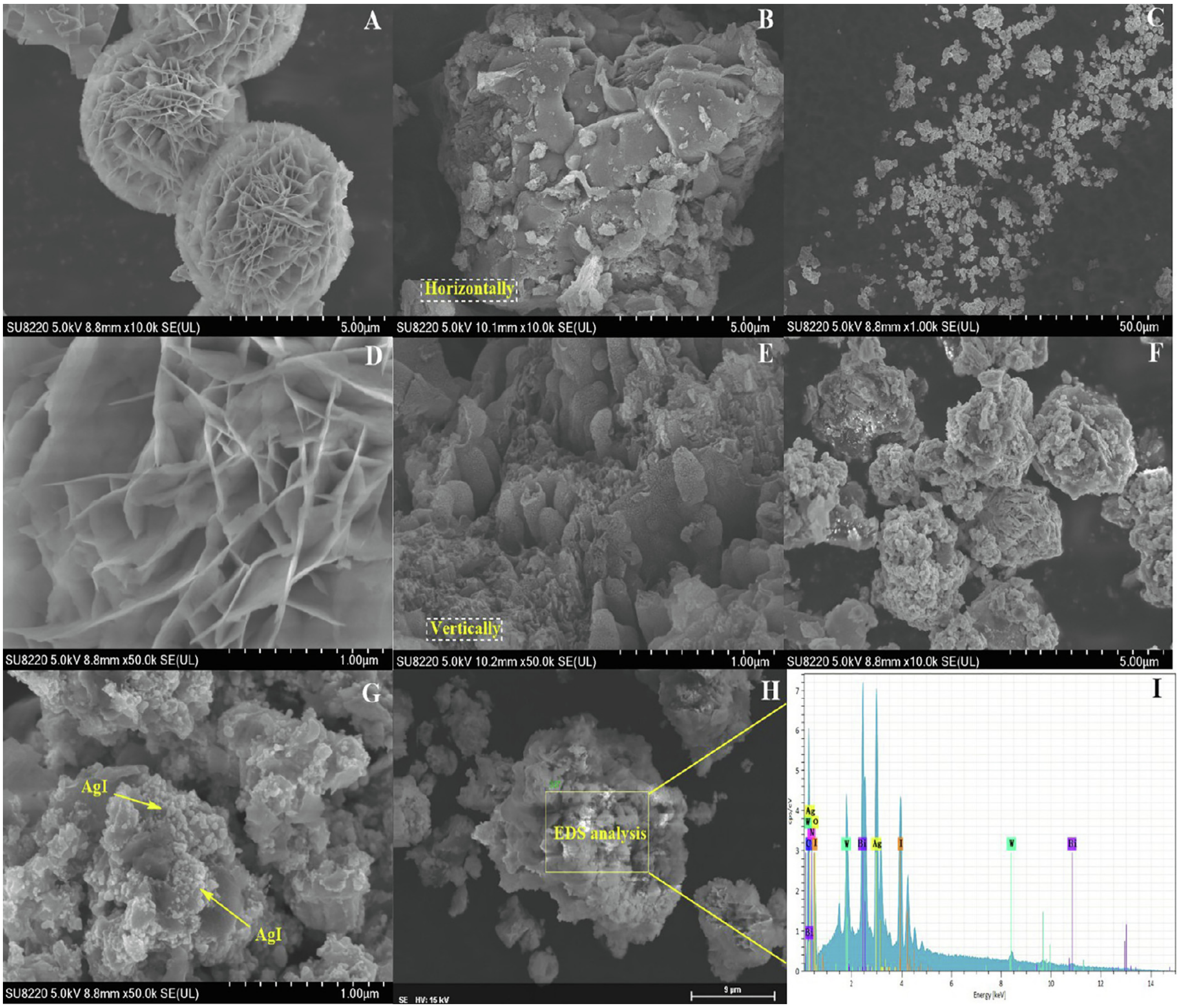

Fig. 2. SEM images of the as-prepared samples: (A, D) Bi_2WO_6, (B, E) g-C_3N_4, (C) AgI, (F-H) CBA composite, and the accompanying EDS image of (I) CBA composite (the marked area of (H)).

could be observed, suggesting the successful incorporation of these samples (Fig. 1A and B). In addition, the diffraction peak located at 13.10° correspond to the (1 0 0) crystal plane almost invisible owing to the low crystallinity of g-C_3N_4 [39]. While, it was observed that there were some special peaks for CB and AB samples (Fig. 1A). It was inferred that the appearance of diffraction peaks located at ≈19 and 24° for the CB sample and at ≈50 and 52° for the CB and AB samples might be due to the purity of the sample was not high enough.

The morphology of as-prepared catalysts was detected by SEM images. From Fig. 2A and D, pure Bi_2WO_6 had an about 4 µm-diameter flower-like microspheres assembled by numerous two-dimensional nanosheets (thickness: 20–40 nm). g-C_3N_4 exhibited slate-like on the horizontally level (Fig. 2B), and from vertically level, it was layered structure formed by stacking nanosheets (Fig. 2E), which represent the special structure property of g-C_3N_4 constructed via the polymerization procedure [40]. The SEM image of AgI displayed irregular nanoparticles and the particle sizes was about 200–400 nm (Fig. 2C). As shown in Fig. 2F, the CBA composite displayed the agglomeration structures which was similar shape compared to the pure Bi_2WO_6 after decorated with g-C_3N_4 and AgI. The chemical procedure to prepare the CB composite based on this principle: $Bi(NO_3)_3$ and g-C_3N_4 nanosheets were dissolved in nitric acid solution with magnetic stirring for 1 h, the Bi^{3+} ions were uniformly adsorbed on g-C_3N_4 nanosheets surface due to the electronegativity characteristics of g-C_3N_4, then, Bi^{3+} ions could react with WO_4^{2-} to generate Bi_2WO_6 microspheres. In addition, Fig. 2G revealed that the particle size of AgI particles in CBA composite was smaller size than that of pure AgI, which may be due to the gigantic surface area provided by the g-C_3N_4 nanosheets that prevented the aggregation of AgI (Fig. S1) [38]. Furthermore, the Bi, W, O, C, N, Ag, and I elements could be found in the EDS image of CBA composite (Fig. 2I). The miscrostructures of catalysts were detected by TEM image. From Fig. 3A, it was observed that Bi_2WO_6 microspheres and AgI nanoparticles were randomly anchored on g-C_3N_4 surface with high dispersion and existed tight link among Bi_2WO_6, g-C_3N_4, and AgI. This tight coupling is favorable for the charge transfer among them and promotes the separation of photogenerated carriers, subsequently improving the photocatalytic activity. HRTEM was adopted to test the lattice fringes of CBA composite. As shown in Fig. 3B, g-C_3N_4 presented an amorphous structure, and that was mainly due to the indistinct in-plane diffraction (1 0 0) in XRD pattern, so the two-dimensional ordering of g-C_3N_4 was very weak and it was hard to find the lattice fringe of g-C_3N_4 [41,56,57]. Meanwhile, the crystal lattice fringes of 0.193 nm, 0.195 and 0.223 nm corresponded to the (2 2 0) plane of Bi_2WO_6, (1 1 2) and (1 1 0) plane of AgI, respectively. The HRTEM of the CBA composite exhibited the typical (2 2 0) plane of Bi_2WO_6, (1 1 2) and (1 1 0) plane of AgI and amorphous g-C_3N_4, which demonstrated the coexistence of Bi_2WO_6, g-C_3N_4 and AgI.

XPS spectra can provide a deeper sight into the surface element compositions and bonding configuration of the CBA ternary composite. The survey XPS spectra of CBA exhibited the peaks of Ag, I, C, N, Bi, W,

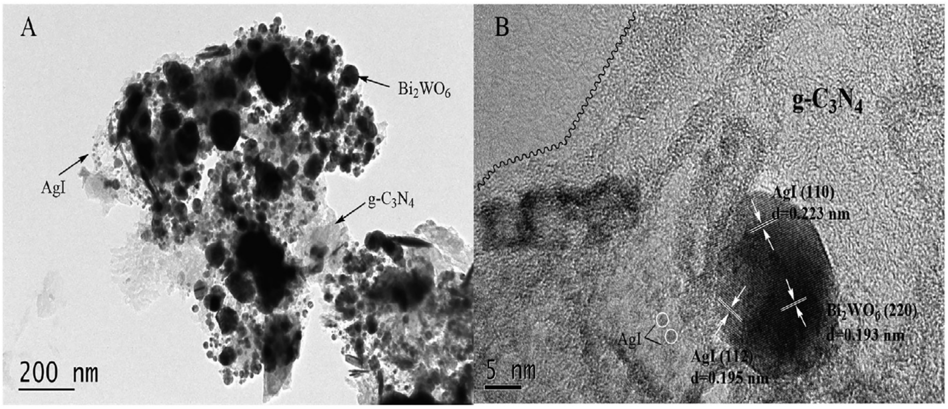

Fig. 3. TEM image of the CBA composite (A), and HRTEM image of the CBA composite (B).

and O elements (Fig. 4A), which was in accord with the results of XRD and EDS. Peaks located at 367.6 and 373.5 eV were assigned to Ag $3d_{5/2}$ and Ag $3d_{3/2}$ respectively (Fig. 4B), which confirmed the existence of Ag^+ in the composite material and no Ag^0 was observed [42]. For I 3d (Fig. 4C), the peaks seated at 618.8 and 630.2 eV were respectively correspond to I $3d_{5/2}$ and I $3d_{3/2}$ which represented the I^- [38]. The peaks at 284.8 and 287.9 eV related to C 1s were displayed the C—C bonds and the sp^2-hybridized carbon (Fig. 4D) [43]. The N 1s spectrum was shown in Fig. 4E, of which the peak at 398.7 eV was related to C—N=C species, while the peak at 400.1 eV was ascribed to the $N\text{-}(C)_3$ groups [44]. The Bi 4f spectra of CBA could be separated into two peaks situated at 159.4 and 164.8 eV respectively, which attributed to Bi $4f_{7/2}$ and Bi $4f_{5/2}$ orbits of Bi^{3+} (Fig. 4F) [45]. Two peaks situated at 35.6 and 37.8 eV were correlated with W $4f_{7/2}$ and W $4f_{5/2}$, indicating the existence of W^{6+} oxidized state (Fig. 4G) [45]. As depicted in Fig. 4H, two peaks at 530.8 and 531.9 eV of O 1s were ascribed to the lattice oxygen of Bi-O and W-O in the form of $[WO_4]^{2-}$ and $[Bi_2O_2]^{2+}$, respectively [46]. The XPS analysis obtained coincide with the experimental data of XRD, SEM and TEM. $g-C_3N_4$ and AgI were intimately contacted with Bi_2WO_6, which was good for the transfer of photogenerated charge in the process of photocatalytic oxidation. All above results and analysis confirm that the $g-C_3N_4/Bi_2WO_6/AgI$ has been successfully synthesized in this work, their special structure may display a decisive role in improving photocatalytic activity.

UV–vis diffuse reflectance spectra were used to study the optical absorption property of the catalysts. From Fig. 5A, the absorption band threshold of Bi_2WO_6, $g-C_3N_4$, and AgI was about 450, 475, and 460 nm, respectively. After the addition of $g-C_3N_4$ and AgI, the CBA composite exhibited a stronger absorption capacity in the visible region, showing more visible light could be adopted to generate photogenerated electrons and holes. Due to the enhanced visible light absorptions, the composite could possess striking visible photocatalytic activity. Thus, this result also further showed that coupling $g-C_3N_4$ and AgI could significantly improve the photocatalytic properties of Bi_2WO_6.

In general, the absorption bandgap (E_g) of Bi_2WO_6, $g-C_3N_4$, and AgI could be evaluated following the Kubelka-Munk equation [47].

$$\alpha hv = A(hv - E_g)^{n/2} \tag{1}$$

where α is the absorption coefficient, h is the planck constant, v displays the light frequency, A and E_g represent a frequency-independent constant and band gap energy, respectively. The n value of Bi_2WO_6 and AgI was both 1 for the direct transition type [42,48]. While, the n value of $g-C_3N_4$ was 4 for the indirect transition type [43]. Thus, as displayed in Fig. 5B–D, the band gaps values for the Bi_2WO_6, $g-C_3N_4$, and AgI were about 2.78, 2.72, and 2.73 eV, respectively.

3.2. Photocatalytic performance study

The photocatalytic performance of as-prepared catalysts was evaluated through the degradation of three single antibiotics (TC, CIP, and ENR) in aqueous solution. As displayed in Fig. 6A–C, the photodegradation of TC, CIP, and ENR was negligible in the absence of catalyst, indicating that those antibiotics were difficultly degraded by sunlight. The concentration of pollutants gradually decreased with the light exposure time increasing for all photocatalyst. Only about 50.90% of TC was decomposed when pure Bi_2WO_6 exists due to its low visible light absorption property and separation efficiency of photogenerated charge (Fig. 6A). While, 46.33% and 60.36% degradation occurred with $g-C_3N_4$ and AgI addition after 60 min irradiation, respectively (Fig. 6A). Bi_2WO_6-based binary and ternary composites existed boosted photocatalytic activity compared with single sample. The TC degradation efficiency of CB and AB were 76.25% and 82.16% under the identical conditions. Especially, the CBA composite exhibited superior photocatalytic performance, and the degradation efficiency towards TC reached about 91.13% under the identical condition (Fig. 6A). Moreover, the degradation of CIP and ENR was exactly like that of TC, and the degradation efficiency of photocatalysts was observed following the orders: $g-C_3N_4 < Bi_2WO_6 <$ AgI < CB < AB < CBA. Compared to pure Bi_2WO_6, the degradation efficiency of CIP and ENR over CBA composite increased by 36.87% (Fig. 6B) and 39.42% (Fig. 6C), respectively. Corresponding, the CIP and ENR removal of CBA were 86.72% and 84.92% within 60 min photodegradation. The order of degradation activity of different antibiotics was as follows: TC > CIP > ENR. Among the three antibiotics, TC has the highest degradation efficiency. This is mainly because floxacin antibiotics contain F, the main mechanism of defluorination is hydroreduction defluorination, while the general catalytic reaction is oxidation reaction [50]. Moreover, there are many phenyl hydroxyl groups in the tetracycline ring, which are easily broken by the attack of oxidizing groups [55]. Therefore, the degradation activity of TC is the highest. The improved photocatalytic activity of CBA was the result of the enhanced light absorption capability and separation and transfer efficiency of photogenerated carriers which was approved by UV–vis spectra, photocurrent response, and EIS tests. The results confirmed the synergistic effects among Bi_2WO_6, $g-C_3N_4$ and AgI, which drastically improved the photocatalytic activity.

We investigated the kinetics of photocatalytic TC, CIP, and ENR degradation by the as-prepared samples using the pseudo-first-order (Eq. (2)) and pseudo-second-order (Eq. (3)) models as follow:

$$-\ln(C_t/C_0) = k_1 t \tag{2}$$

$$1/C_t - 1/C_0 = k_2 t \tag{3}$$

where k_1 (min^{-1}) is the apparent rate constant of pseudo-first-order kinetics and k_2 ($L\ mg^{-1}\ min^{-1}$) is the apparent rate constant of pseudo-

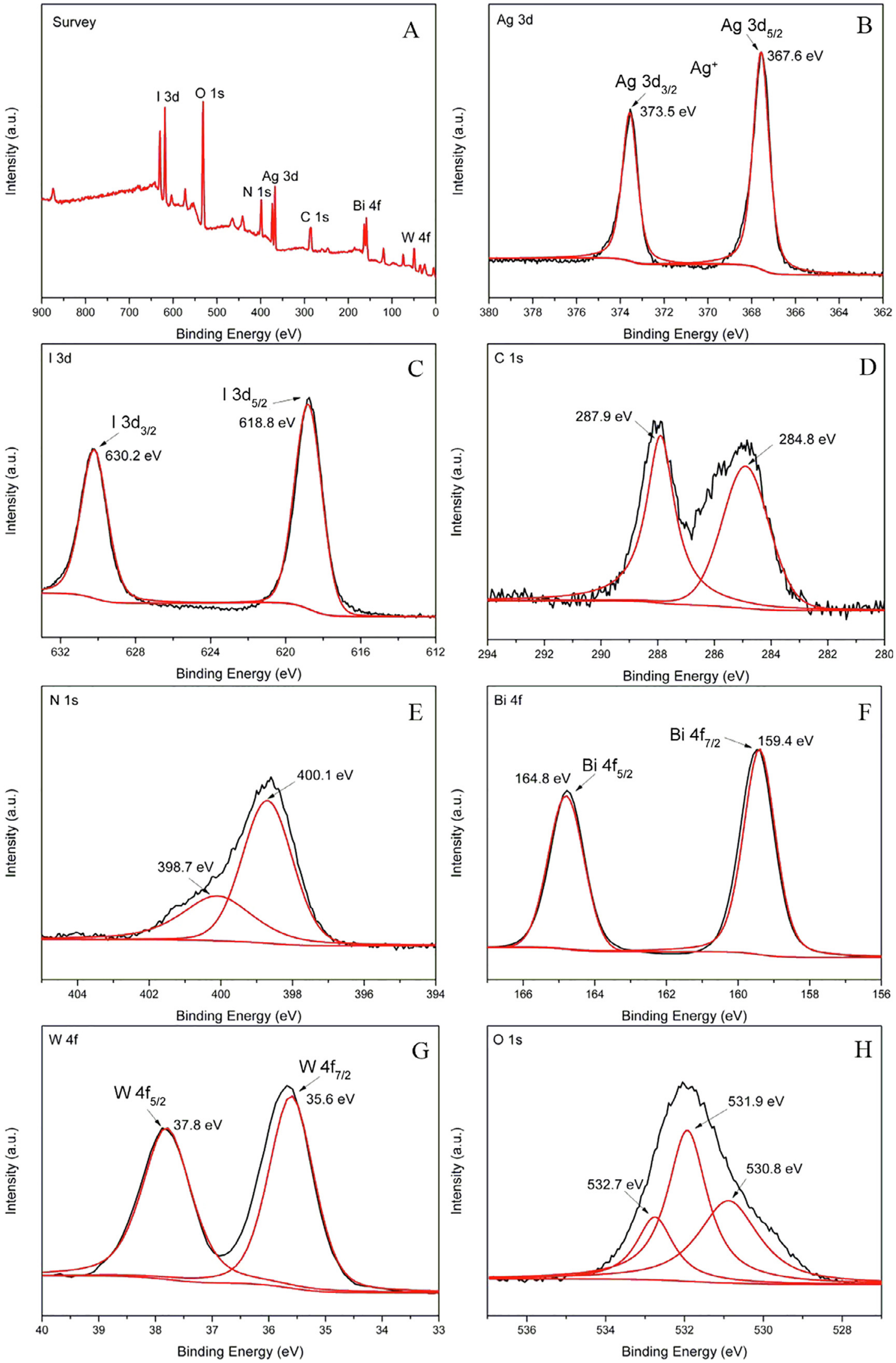

Fig. 4. XPS spectra of the CBA composite: (A) survey, (B) Ag 3d, (C) I 3d, (D) C 1s, (E) N 1s, (F) Bi 4f, (G) W 4f and (H) O 1s.

second-order kinetics, C_0 and C_t are the pollutant concentrations at reaction time 0 and t, respectively. The linear fitting data of these two kinetics models were displayed in Fig. S2 and Fig. 6 and the corresponding apparent rate constants were listed in Table 1, Tables S1 and S2, respectively. The correlation coefficients (R^2) demonstrated that the pseudo-second-order model was fitted better to describe the

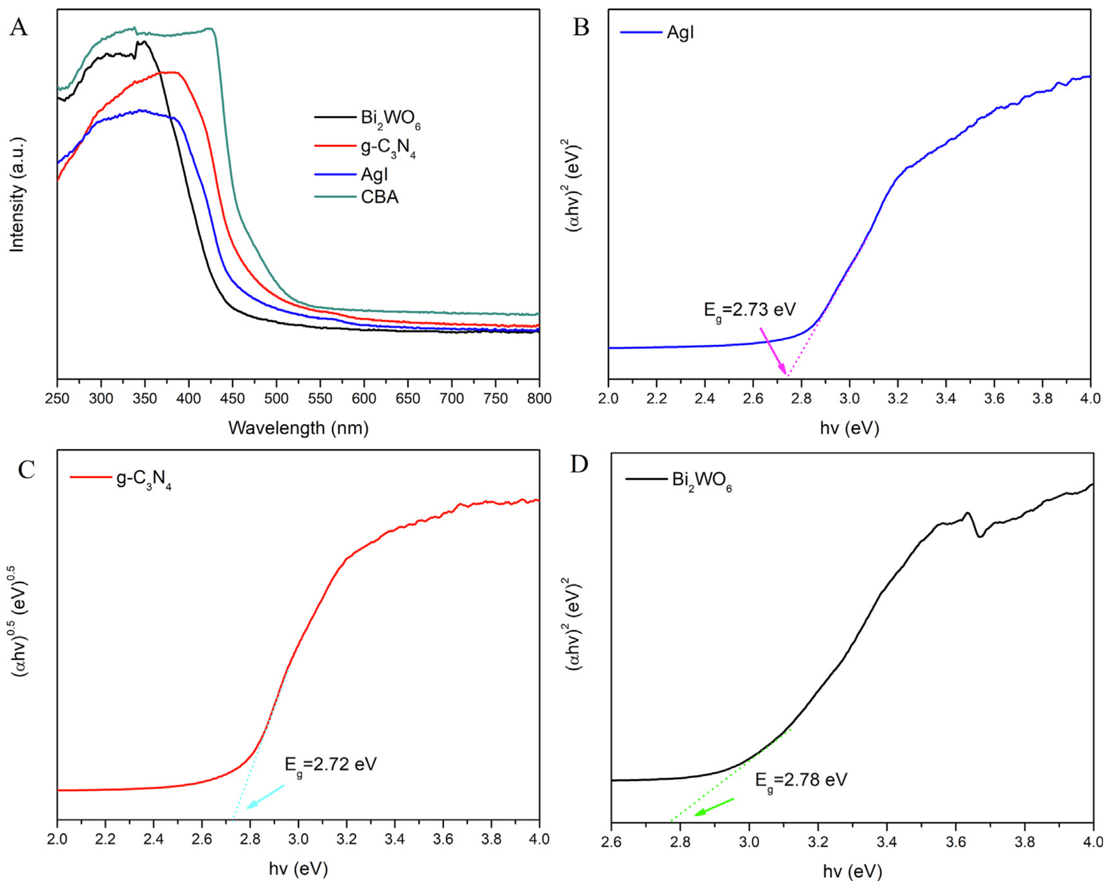

Fig. 5. (A) UV–vis diffuse reflectance spectra of Bi_2WO_6, g-C_3N_4, AgI, and CBA; (B, C, D) The calculated bandgap of AgI, g-C_3N_4, and Bi_2WO_6, respectively.

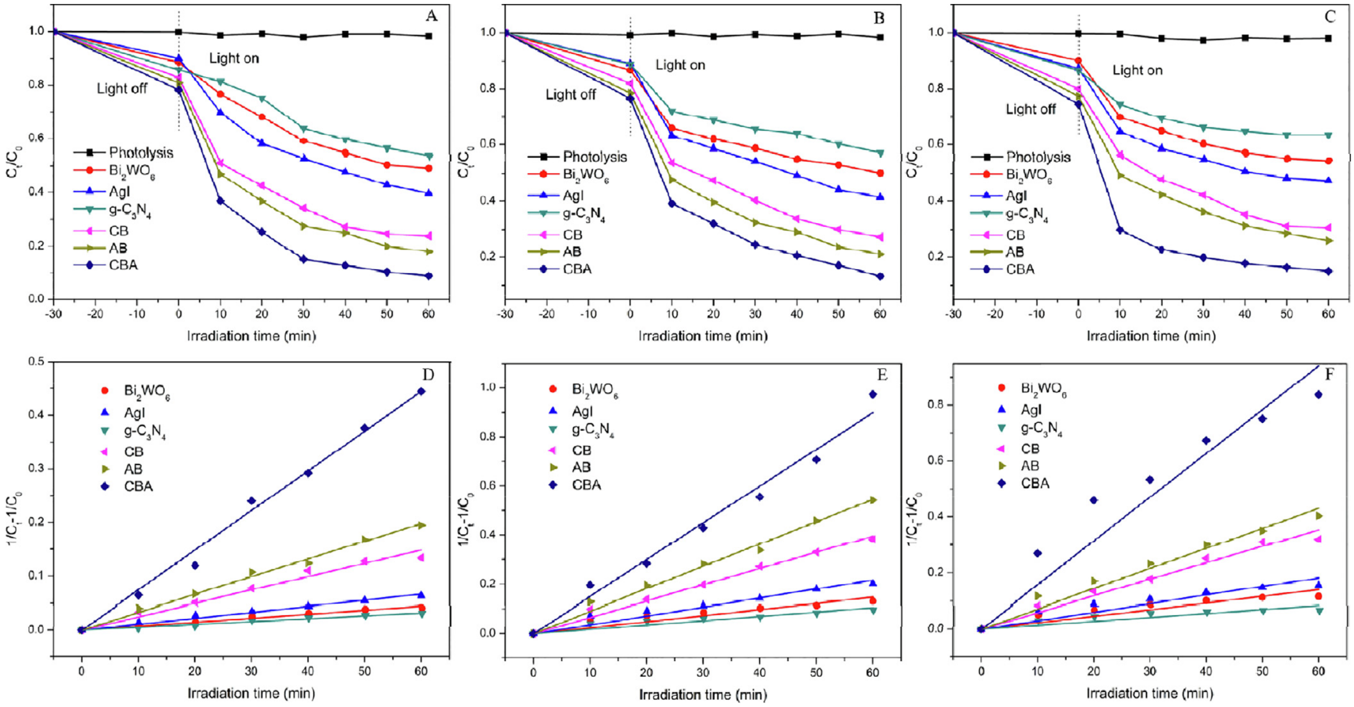

Fig. 6. (A) Photodegradation of (A) TC, (B) CIP, and (C) ENR by using different samples under visible light irradiation; (D, E, F) The pseudo-second-order kinetics of TC, CIP, and ENR degradation, respectively.

photocatalytic process of TC, CIP, and ENR removal than the pseudo-first-order model. It was observed that the CBA composite had the maximum reaction rate constant of TC, which reached 10.04, 13.94 and 6.73 times higher than Bi_2WO_6, g-C_3N_4 and AgI, respectively (Table 1). The rate constants of CIP and ENR over the CBA were 1.50×10^{-2} and 1.57×10^{-2} L mg^{-1} min^{-1} (Tables S2 and S3, respectively).

Table 1
Apparent rate constants of photocatalytic TC degradation from pseudo-first-order and pseudo-second-order models.

Sample	Pseudo-first-order kinetics		Pseudo-second-order kinetics	
	k_1 (min^{-1})	R^2	k_2 (L mg^{-1} min^{-1})	R^2
Bi_2WO_6	1.01×10^{-2}	0.9572	7.37×10^{-4}	0.9933
g-C_3N_4	8.46×10^{-3}	0.9647	5.31×10^{-4}	0.9892
AgI	1.3×10^{-2}	0.9440	1.10×10^{-3}	0.9943
CB	2.02×10^{-2}	0.9080	2.46×10^{-3}	0.9910
AB	2.37×10^{-2}	0.9249	3.29×10^{-3}	0.9977
CBA	3.49×10^{-2}	0.9114	7.40×10^{-3}	0.9970

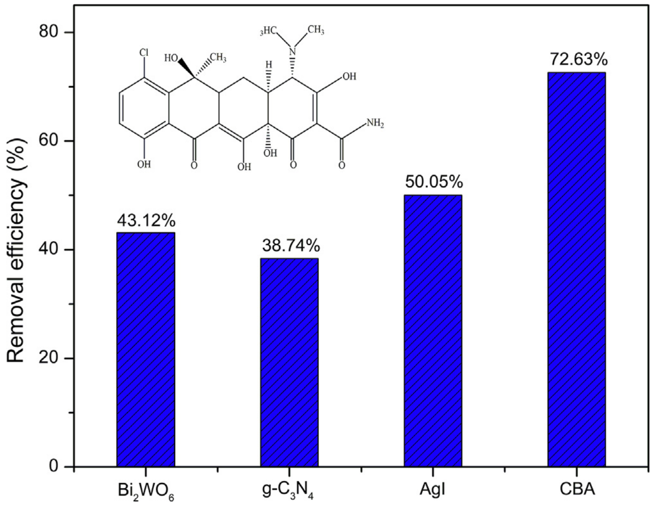

Fig. 8. TOC removal by Bi_2WO_6, g-C_3N_4, AgI and CBA within 90 min irradiation.

Therefore, we confirmed that it should be more suitable to describe the photodegradation reaction of the as-prepared samples as the pseudo-second-order kinetics reaction [62,63]. The above results indicated that the photocatalytic performance of Bi_2WO_6 was significantly enhanced because of the construction of g-C_3N_4/Bi_2WO_6/AgI ternary composite.

In addition, the photostability of the CBA ternary composite was evaluated with TC degradation via a cycling experiment. As presented in Fig. 7A, the degradation efficiency of TC respectively was 91.13%, 90.34%, 88.98%, and 86.15% for 1st, 2nd, 3rd, and 4th run. The photodegradation efficiency only decreased by 4.98%, showing the excellent photostability of the CBA composite. Generally, pure AgI is unstable and Ag^+ is easy to be reduced in visible light. To confirm the photostability of the CBA composite, the used CBA composite was analyzed by XRD and XPS, respectively. As revealed in Fig. 7B, the XRD pattern of the used CBA composite was almost no visible difference from the fresh CBA, and no peaks was attributed to Ag^0. From Fig. 7C, the Ag $3d_{5/2}$ and Ag $3d_{3/2}$ of the used CBA could only be divided into two peaks at 367.8 and 373.7 eV, which represented the characteristic

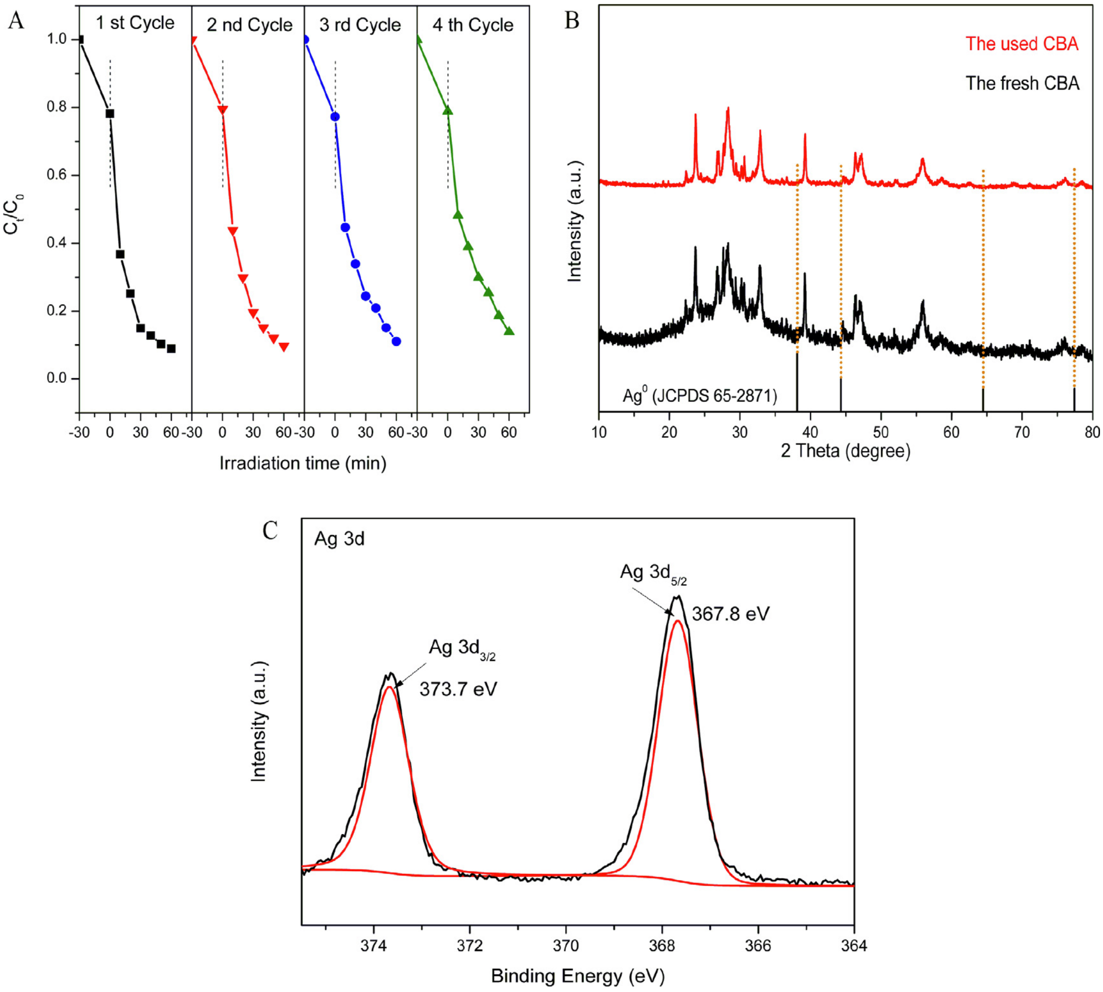

Fig. 7. (A) Cycling photocatalytic test of the CBA composite; (B) XRD patterns of the CBA composite before and after photocatalytic tests; (C) Ag 3d XPS spectra of the used CBA after photoreaction.

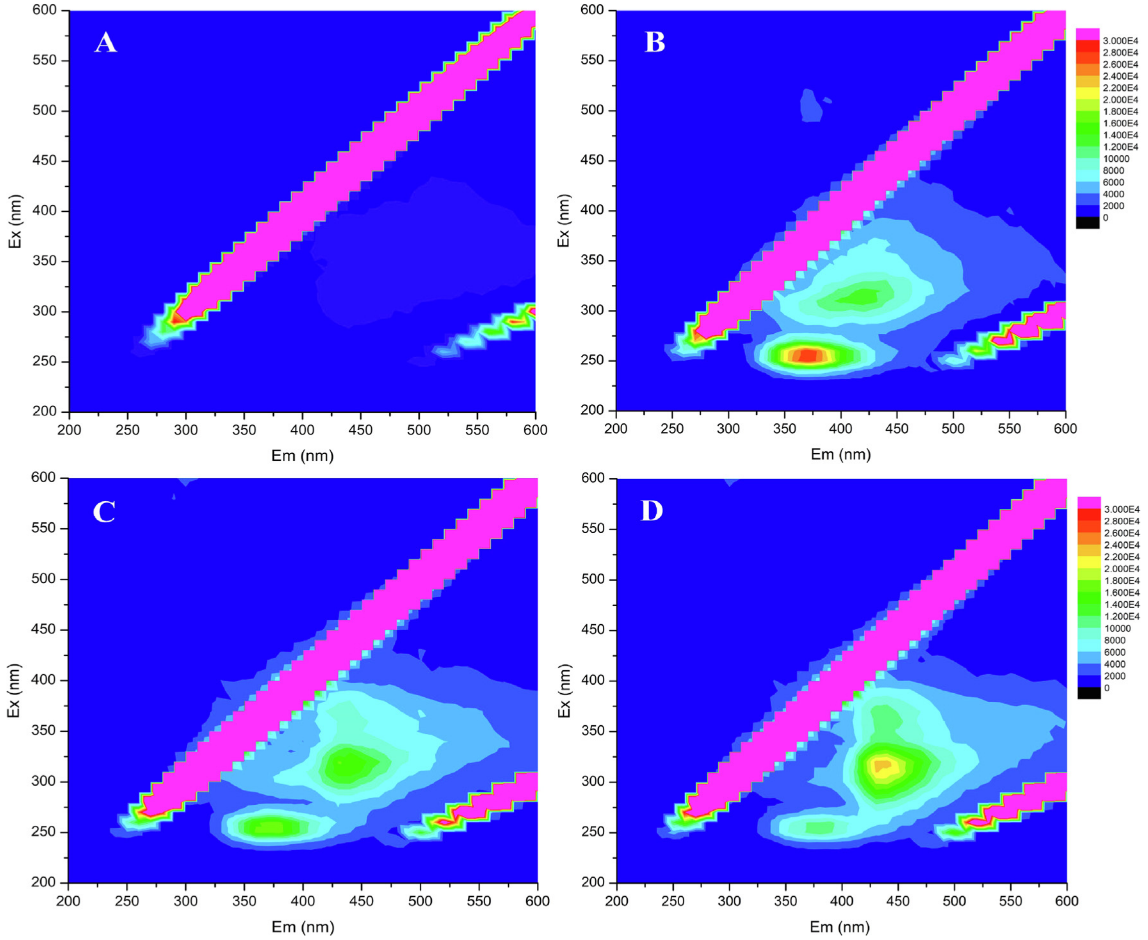

Fig. 9. 3D EEMs of the TC aqueous solution: (A) taken from the original solution; (B-D) obtained after an irradiation time of 30, 60, and 90 min, respectively.

peak of Ag^+. The results above demonstrated that Ag^+ was not be reduced and CBA possessed favorable chemical stability during use. The possible explanation was that the construction of $g-C_3N_4/Bi_2WO_6/AgI$ heterojunction could accelerate the transfer of electrons on the surface of AgI [42], or the relatively lower loading amount of AgI (20%) because of the carriers transfer path might be changed by different dominant components [47].

3.3. Evaluations of mineralization activity toward TC degradation

Generally, the mineralization ability of catalyst was weaker than the degradation efficiency, owing to the formation of intermediates. Fig. 8 revealed the degradation efficiency of TC in the photocatalytic process based on TOC removal by Bi_2WO_6, $g-C_3N_4$, AgI and CBA composite within 90 min irradiation. The TOC removal efficiencies for Bi_2WO_6, $g-C_3N_4$, AgI and CBA were 43.12%, 38.74%, 50.05% and 72.63%, which was similar to the photodegradation data. The obtained results above suggested that the CBA composite displayed superior photocatalytic activity and mineralization effectively for TC degradation. 3D EEMs analysis was also utilized to further study the degradation process of TC by CBA composite. From Fig. 9A, no extra signals presented in original TC solution. After irradiation of 30 min (Fig. 9B), two obvious fluorescence peaks located at E_x/E_m = 235–255/350–380 nm and E_x/E_m = 285–330/375–465 nm occurred, which was attributed to the production of aromatic hydrocarbons and humic acids-like matters, respectively [49]. The results above demonstrated the molecular structure of TC was broken or some intermediates formed in - photocatalytic reaction process. When the irradiation time increased to 90 min (Fig. 9D), the peak strength of aromatics decreased and the peak strength of humic acids-like matters increased, showing that the TC molecules continued to be degraded by CBA composite. Therefore, 3D EEMs results further showed that the CBA composite displayed excellent mineralization ability toward TC degradation.

3.4. Comparison with other Bi_2WO_6 based photocatalysts

In recent years, some Bi_2WO_6 based photocatalysts have been reported for the photocatalytic degradation of TC, CIP and ENR. In order to examine the efficiency, the comparisons of photocatalytic activities of the CBA with the reported Bi_2WO_6 based photocatalysts are very important. As listed in Table S1, the optimal TC, CIP and ENR removal efficiency of CBA was 91.13%, 86.72% and 84.92% within 60 min, which was preponderant or tolerable when compared with other Bi_2WO_6 based photocatalysts such as $CuInS_2/Bi_2WO_6$ [25], $g-C_3N_4/Bi_2WO_6$ [58], CN/CNT/BWO [59], $Bi_2S_3@Bi_2WO_6/WO_3$ [60], PO_4-doped Bi_2WO_6 [61], etc. The results showed that the CBA composite had great potentials for TC, CIP and ENR removal from contaminated water.

3.5. Photocatalytic degradation mechanism

To elucidate the mechanism of photocatalytic reaction, the main active species were identified by radical trapping experiments over CBA composite. Three quenchers (TEMPOL, IPA and $Na_2C_2O_4$) were added before photodegradation of TC to capture $^{\cdot}O_2^-$, $^{\cdot}OH$ and h^+ radical, respectively [50]. The dosage of these quenchers was 5 mM, and the results were exhibited in Fig. 10. The addition of TEMPOL, IPA, or $Na_2C_2O_4$ all displayed a negative performance impact for the

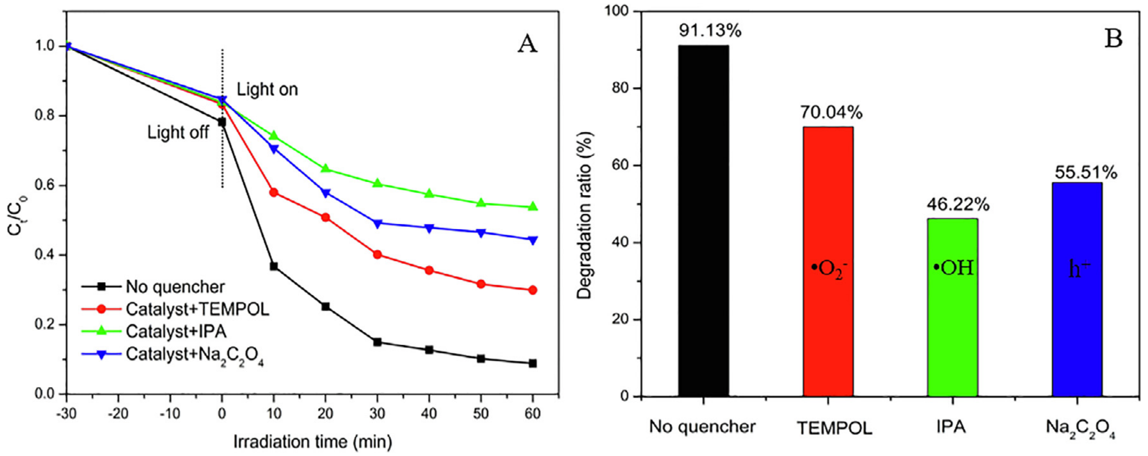

Fig. 10. Effect of different quenchers on the photocatalytic oxidation of TC by CBA composite (A, degradation curve; B, corresponding degradation efficiency).

degradation of TC by CBA composite (Fig. 10A). The degradation efficiency of TC reduced from 91.13% to 70.04% (BQ), 46.22% (IPA), and 55.51% ($Na_2C_2O_4$), respectively (Fig. 10B). Therefore, it could be assumed that $^{\cdot}OH$ displayed a major role for TC degradation, and $^{\cdot}O_2^-$ and h^+ also affected the removal efficiency greatly.

To further validate the radical generation in the photocatalytic system over the CBA composite, the ESR spin-trap technique was conducted. Fig. 11 presented the ESR spectra of Bi_2WO_6 and CBA composite with the DMPO as the trapping agent. As indicated in Fig. 11A and C, the signals of DMPO-$^{\cdot}O_2^-$ were detected obviously for Bi_2WO_6 and CBA composite in visible light, and the peak intensity of CBA was higher than Bi_2WO_6, showing that more $^{\cdot}O_2^-$ radical was produced in the CBA photocatalytic system. While, the generation of $^{\cdot}O_2^-$ radical in Bi_2WO_6 might be due to the reduction of oxygen molecule (O_2) in air through the electrons transfer from bottom to top of CB of Bi_2WO_6 [51]. Similarly, the signals of DMPO-$^{\cdot}OH$ were also obtained in Bi_2WO_6 and CBA composites, and the peak intensity of CBA was also higher than Bi_2WO_6 (Fig. 11B and D). No signals of DMPO-$^{\cdot}O_2^-$ and DMPO-$^{\cdot}OH$ were observed in the dark, demonstrating that the reaction was driven by the photocatalytic process only. Therefore, the ESR analysis confirmed that $^{\cdot}O_2^-$ and $^{\cdot}OH$ radical were generated by both Bi_2WO_6 and CBA composite, and more $^{\cdot}O_2^-$ and $^{\cdot}OH$ radical existed in the CBA

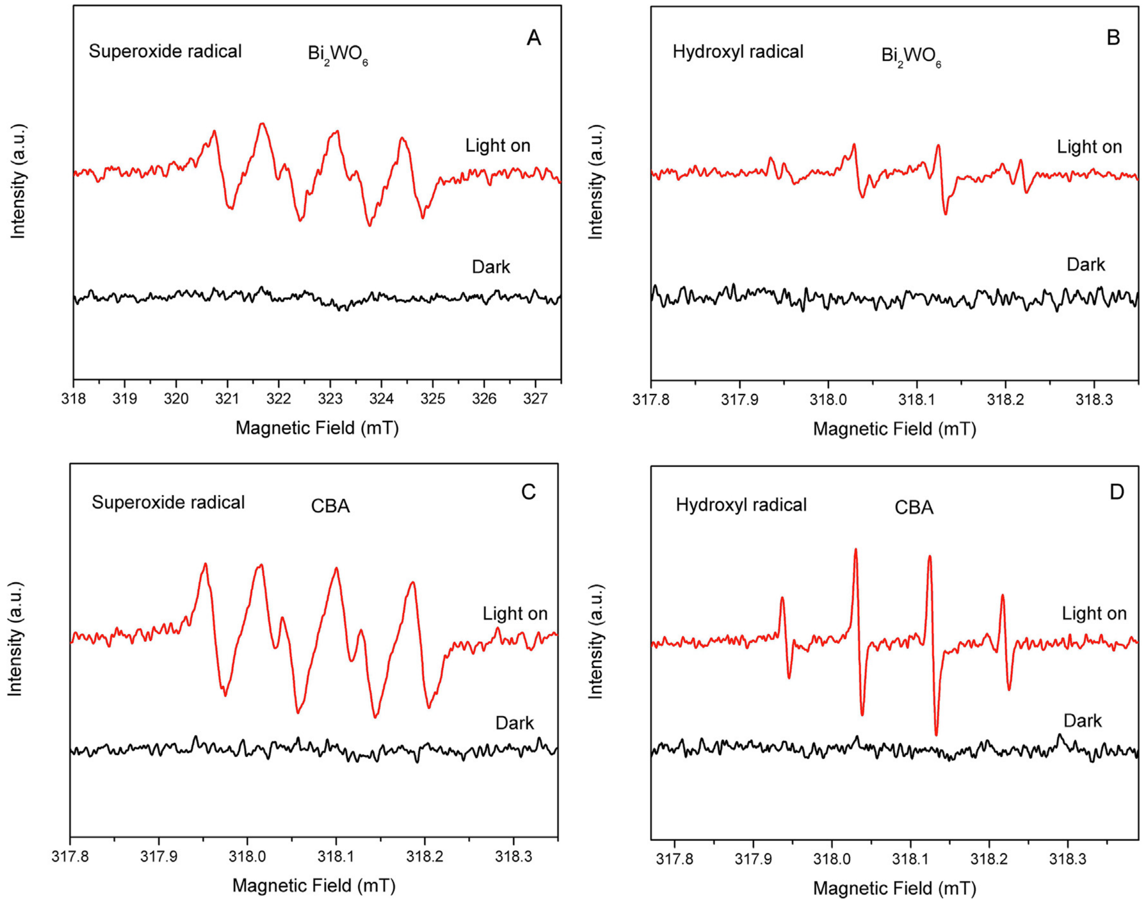

Fig. 11. ESR spectra of radical adducts trapped by DMPO: (A, C) superoxide radical ($^{\cdot}O_2^-$) for Bi_2WO_6 and CBA composite and (B, D) hydroxyl radical ($^{\cdot}OH$) in Bi_2WO_6 and CBA composite in the dark and under visible light irradiation.

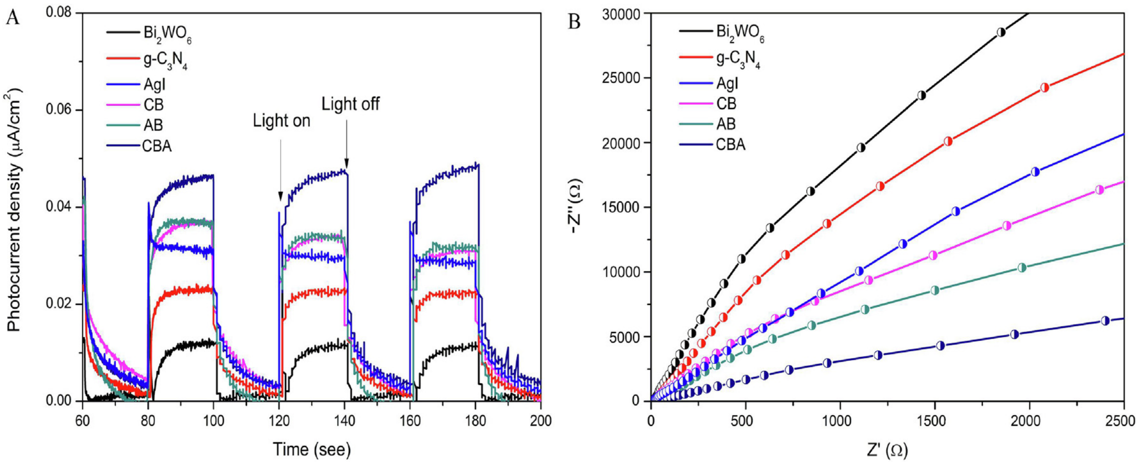

Fig. 12. Photoelectrochemical measurements of samples. (A) Comparison of transient photocurrent response of synthesized samples; (B) EIS Nynquist plots of prepared samples.

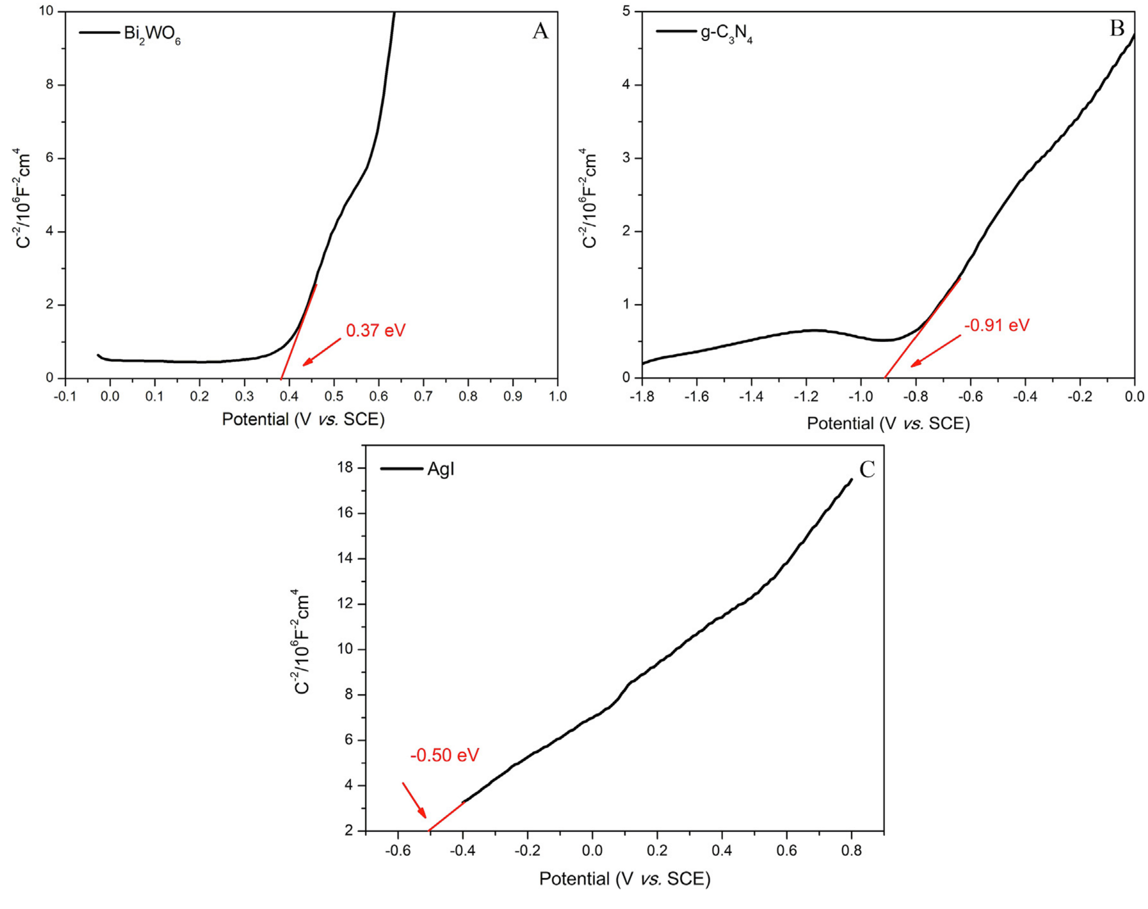

Fig. 13. Mott-Schottky curves of Bi_2WO_6, g-C_3N_4, and AgI, respectively.

reaction system, which could be attributed to the more efficient separation and transfer of photogenerated carriers.

The separation and transfer performance of photogenerated carriers had major impact on the production of radical species, which could be detected by photocurrent response and EIS analysis. The stronger photocurrent intensity shows higher separation efficiency of photogenerated carriers [28,34]. Fig. 12A presented the photocurrent response of synthesized samples under visible light irradiation with light on-off cycles (λ > 420 nm). All samples presented a stable photocurrent intensity, and the intensity value of CBA was the strongest (~1.21 μA/cm^2), which was about 4.65-fold higher than Bi_2WO_6 (~0.26 μA/cm^2). It confirmed that CBA possessed an enhanced carriers separation efficiency. EIS Nynquist plots provides a definitive evidence for investigating the interfacial charge transfer property of as-prepared samples [28,50]. It is always been known that the smaller arc radius shows the lower impedance and higher efficient charge transfer [30]. In Fig. 12B, the arc radius sequence of those samples was presented as follows: Bi_2WO_6 > g-C_3N_4 > AgI > CB > AB > CBA. Apparently, the CBA composite displayed the smallest arc radius among those samples, showing optimum electronic conductivity due to the tight connection achieved by g-C_3N_4 and AgI facilitated the interfacial charge transfer of CBA composite. According to the results of photocurrent and

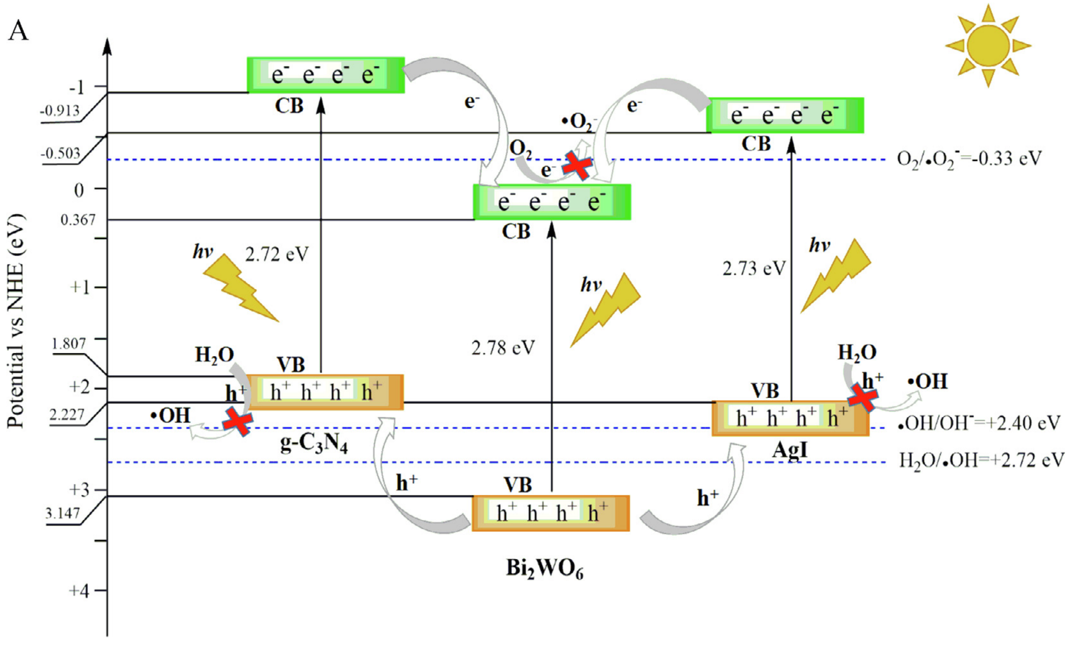

Conventional heterojunction

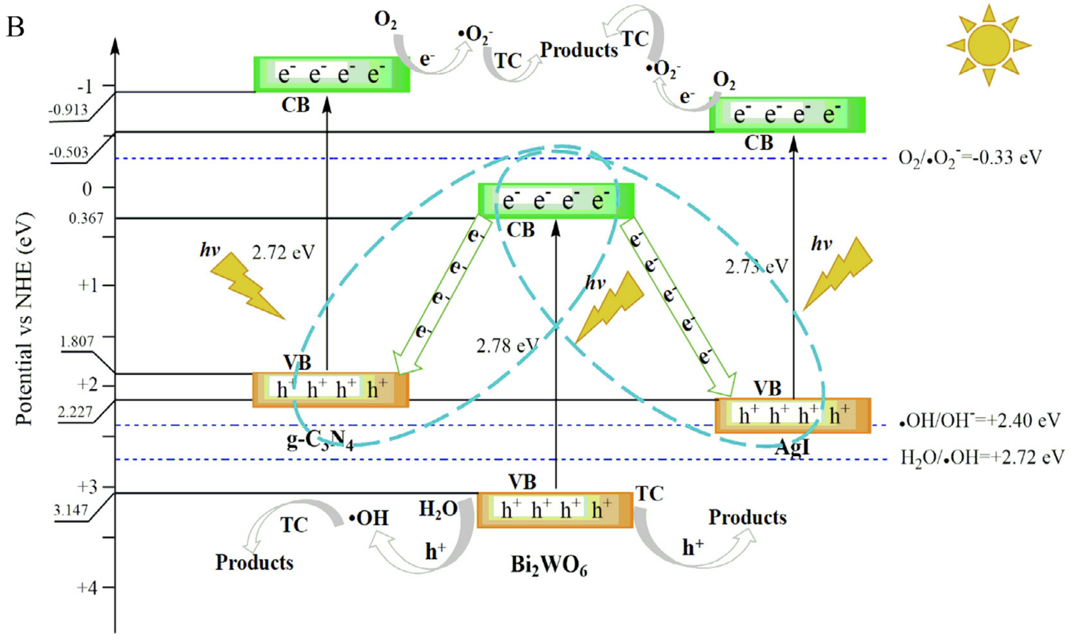

Dual Z-scheme heterojunction

Scheme 1. The photocatalytic reaction and charge transfer mechanism of the CBA ternary photocatalyst under visible light irradiation (A, B).

EIS, it could further demonstrate that the CBA composite possessed highly efficient separation and transfer capability of photogenerated carriers.

The flat band potential of Bi_2WO_6, g-C_3N_4, and AgI was determined with Mott-Schottky measurements and could be confirmed through the following expression [52]:

$$\frac{1}{C^2} = \frac{2}{q\varepsilon\varepsilon_0 N_d}\left(E - E_{fb} - \frac{K_bT}{q}\right) \tag{4}$$

where ε and ε_0 represent the dielectric constants of the sample and permittivity of vacuum, and N_d, C, E, T, q and K_b, are the donor density, space charge capacitance, applied potential, temperature, electronic charge, and Boltzmann's constant, respectively. The E_{fb} of Bi_2WO_6, g-C_3N_4, and AgI was estimated to be 0.37, −0.91, and −0.50 eV versus an Ag/AgCl electrode (Fig. 13), corresponding with 0.567, −0.713, and −0.303 eV versus the normal hydrogen electrode, respectively. Moreover, the positive slope of the Mott-Schottky curve shows that they are all n-types semiconductors. In general, the E_{fb} of n-type semiconductor material is located 0.2 eV below the CB potential [53]. Therefore, the CB of Bi_2WO_6, g-C_3N_4, and AgI was calculated to be 0.367, −0.913, and −0.503 eV, and their VB potentials were determined to be 3.147, 1.807, and 2.227 eV, respectively.

Thus, the possible degradation mechanisms over ternary CBA composite with visible light excitation was raised (Scheme 1). There were two possible charge transfer pathways for CBA composite. As presented in Scheme 1A, under visible light irradiation, Bi_2WO_6, g-C_3N_4, and AgI could all be stimulated and generated electrons (e^-) and holes (h^+). Owing to the less negative CB potential of Bi_2WO_6 than that of g-C_3N_4 and AgI, and the less positive VB of g-C_3N_4 and AgI than that of Bi_2WO_6, the photogenerated e^- in the CB of g-C_3N_4 and AgI would migrate to the Bi_2WO_6, the photogenerated h^+ in the VB of Bi_2WO_6 would transfer to the g-C_3N_4 and AgI, resulting in the separation of photogenerated e^- and h^+. While, the h^+ accumulated in the VB of g-C_3N_4 and AgI could not power oxidize OH^- or H_2O to $^{\cdot}OH$ because the VB potentials of g-C_3N_4 and AgI were more negative than the $^{\cdot}OH/OH^-$ potential (+2.40 eV vs. NHE) and $H_2O/^{\cdot}OH$ (+2.72 eV vs. NHE) [17,54]. Moreover, the photogenerated e^- in the CB of Bi_2WO_6 could reduce O_2 to $^{\cdot}O_2^-$ due to the e^- transferring from bottom to top of CB of Bi_2WO_6 instead of the e^- of the CB bottom of Bi_2WO_6 as the redox potential for O_2 into $^{\cdot}O_2^-$ is −0.33 eV [55]. Therefore, in this case, $^{\cdot}O_2^-$ and $^{\cdot}OH$ were not be produced in the degradation process, which was not in step with the results of radical trapping experiments and ESR results. Therefore, it might not be true to determine the transfer way of photogenerated carriers in CBA ternary composite followed the traditional heterojunction model. The direct dual Z-scheme mechanism was the more suitable one (Scheme 1B). Under visible light, the photogenerated e^- formed on the CB of Bi_2WO_6 would recombine with the h^+ from the VB of g-C_3N_4 and AgI, leading to the efficient separation of photogenerated electron-hole pairs. The migration of photogenerated carriers could result in the e^- retaining at the CB of g-C_3N_4 and AgI, and the h^+ accumulated at the VB of Bi_2WO_6, respectively. Thus, the photogenerated e^- in the CB of g-C_3N_4 (−0.913 eV) and AgI (−0.503 eV) could reduce O_2 to $^{\cdot}O_2^-$ because their CB potentials were more negative than the potential of $O_2/{\cdot}O_2^-$ (−0.33 eV vs. NHE). The photogenerated h^+ in the VB of Bi_2WO_6 (3.147 eV) could activate H_2O molecules to form $^{\cdot}OH$ or oxidation of organic pollutants, owing to the potential of VB of Bi_2WO_6 was less negative than that of $H_2O/^{\cdot}OH$ (+2.72 eV vs. NHE). The above result and analysis were coincided with the results of radical trapping experiments and ESR analysis. Therefore, it could be determined that the photocatalytic reaction of CBA heterojunction photocatalyst followed a direct dual Z-scheme transfer system, which could enhance the separation and transfer efficiency of photogenerated carriers as well as maintain the strong redox capability for high efficient degradation of pollutants.

4. Conclusions

In sum, a novel ternary g-C_3N_4/Bi_2WO_6/AgI heterojunction photocatalyst with a direct dual Z-scheme configuration was successfully synthesized through the hydrothermal reaction of Bi_2WO_6 and g-C_3N_4 and a succedent in-situ precipitation route. The ternary CBA composite displayed superior photocatalytic performance for multiple antibiotics degradation. The degradation efficiency of TC, CIP, and ENR by CBA composite increased by 40.23%, 36.87%, and 39.42% compared with pure Bi_2WO_6, respectively. Meanwhile, 72.63% of TOC degradation was achieved within 90 min, indicating the CBA photocatalyst exhibited good mineralization ability for TC degradation and further revealed by 3D EEMs. The introduction of g-C_3N_4 and AgI results in the improved light absorption properties of the CBA composite. Moreover, the intimate contact of Bi_2WO_6, g-C_3N_4, and AgI promotes the transfer of photogenerated carriers, raising the separation efficiency, and more photogenerated electrons and holes could participate in the degradation of pollutants. Trapping experiments and ESR analysis validated the significant role $^{\cdot}O_2^-$, h^+ and $^{\cdot}OH$ displayed in the course of photodegradation process. Mechanistic studies demonstrated that the carriers transfer of the g-C_3N_4/Bi_2WO_6/AgI composite photocatalyst followed a direct dual Z-scheme but not conventional heterojunction system. Furthermore, this ternary photocatalyst displays good reusability and stability. This study highlights a new method to construct a multicomponent Z-scheme heterojunction photocatalysts for energy utilization and environmental remediation.

Acknowledgements

This work was financially supported by Hunan Provincial Innovation Foundation For Postgraduate (CX2018B196), the Program for the National Natural Science Foundation of China (51879101, 51579098, 51779090, 51709101, 51521006, 51809090, 51278176, 51378190), the National Program for Support of Top-Notch Young Professionals of China (2014), the Program for Changjiang Scholars and Innovative Research Team in University (IRT-13R17), and Hunan Provincial Science and Technology Plan Project (2018SK20410, 2017SK2243, 2016RS3026), and the Fundamental Research Funds for the Central Universities (531119200086, 531118010114, 531107050978).

Appendix A. Supplementary data

Supplementary data to this article can be found online at https://doi.org/10.1016/j.cej.2019.05.069.

References

[1] J.L. Martinez, Environmental pollution by antibiotics and by antibiotic resistance determinants, Environ. Pollut. 157 (2009) 2893–2902.
[2] W. Wang, P. Xu, M. Chen, G. Zeng, C. Zhang, C. Zhou, Y. Yang, D. Huang, C. Lai, M. Cheng, L. Hu, W. Xiong, H. Guo, M. Zhou, Alkali metal assisted synthesis of graphite carbon nitride with tunable band-gap for enhanced visible-light-driven photocatalytic performance, ACS Sustain. Chem. Eng. 6 (2018) 15503–15516.
[3] D. Huang, W. Xue, G. Zeng, W. Jia, G. Chen, H. Chao, Z. Chen, C. Min, P. Xu, Immobilization of Cd in river sediments by sodium alginate modified nanoscale zero-valent iron: impact on enzyme activities and microbial community diversity, Water Res. 106 (2016) 15–25.
[4] S. Park, K. Choi, Hazard assessment of commonly used agricultural antibiotics on aquatic ecosystems, Ecotoxicology 17 (2008) 526–538.
[5] Q. Zhang, G. Ying, C. Pan, Y. Liu, J. Zhao, Comprehensive evaluation of antibiotics emission and fate in the river basins of china: source analysis, multimedia modeling, and linkage to bacterial resistance, Environ. Sci. Technol. 49 (2015) 6772–6782.
[6] W. Xue, Z. Peng, D. Huang, G. Zeng, J. Wan, R. Xu, M. Cheng, C. Zhang, D. Jiang, Z. Hu, Nanoremediation of cadmium contaminated river sediments: Microbial response and organic carbon changes, J. Hazard. Mater. 359 (2018) 290–299.
[7] B. Maliwan, D.W. Hawker, Evaluation of food chain transfer of the antibiotic oxytetracycline and human risk assessment, Chemosphere 93 (2013) 1009–1014.
[8] F. Wang, Y. Feng, P. Chen, Y. Wang, Y. Su, Q. Zhang, Y. Zeng, Z. Xie, H. Liu, Y. Liu, W. Lv, G. Liu, Photocatalytic degradation of fluoroquinolone antibiotics using ordered mesoporous g-C_3N_4 under simulated sunlight irradiation: Kinetics, mechanism, and antibacterial activity elimination, Appl. Catal. B Environ. 227 (2018) 114–122.
[9] L. Yi, M. Daqing, R. Michal, Z. Qixing, Z. Hongjie, X. Lin, J.J.A. Pedro, Trends in antibiotic resistance genes occurrence in the Haihe River, China, Environ. Sci. Technol. 44 (2010) 7220–7225.
[10] D. Huang, Z. Li, G. Zeng, C. Zhou, W. Xue, X. Gong, X. Yan, S. Chen, W. Wang, M. Cheng, Megamerger in photocatalytic field: 2D g-C_3N_4 nanosheets serve as support of 0D nanomaterials for improving photocatalytic performance, Appl. Catal. B Environ. 240 (2019) 153–173.
[11] J. Di, C. Zhu, M. Ji, M. Duan, R. Long, C. Yan, K. Gu, J. Xiong, Y. She, J. Xia, H. Li, Z. Liu, Defect-rich $Bi_{12}O_{17}Cl_2$ nanotubes self-accelerating charge separation for boosting photocatalytic CO_2 reduction, Angew. Chem. Int. Ed. 57 (2018) 14847–14851.
[12] Y. Zhou, Y. Zhang, M. Lin, J. Long, Z. Zhang, H. Lin, J.C.S. Wu, X. Wang, Monolayered Bi_2WO_6 nanosheets mimicking heterojunction interface with open surfaces for photocatalysis, Nat. Commun. 6 (2015) 8340.
[13] Z. Zhang, W. Wang, E. Gao, S. Sun, L. Zhang, Photocatalysis coupled with thermal effect induced by SPR on Ag-loaded Bi_2WO_6 with enhanced photocatalytic activity, J. Phys. Chem. C 116 (2012) 25898–25903.
[14] L. Zhang, H. Wang, Z. Chen, P.K. Wong, J. Liu, Bi_2WO_6 micro/nano-structures: synthesis, modifications and visible-light-driven photocatalytic applications, Appl. Catal. B Environ. 106 (2011) 1–13.
[15] M.S. Gui, W.D. Zhang, Y.Q. Chang, Y.X. Yu, One-step hydrothermal preparation strategy for nanostructured WO_3/Bi_2WO_6 heterojunction with high visible light photocatalytic activity, Chem. Eng. J. 197 (2012) 283–288.
[16] P. Zhou, J. Yu, M. Jaroniec, All-solid-state Z-scheme photocatalytic systems, Adv. Mater. 26 (2014) 4920–4935.
[17] D. Huang, X. Yan, M. Yan, G. Zeng, C. Zhou, J. Wan, M. Cheng, W. Xue, Graphitic carbon nitride-based heterojunction photoactive nanocomposites: applications and mechanism insight, ACS Appl. Mater. Inter. 10 (2018) 21035–21055.
[18] Y. Hong, Y. Jiang, C. Li, W. Fan, Y. Xu, M. Yan, W. Shi, In-situ synthesis of direct solid-state Z-scheme V_2O_5/g-C_3N_4 heterojunctions with enhanced visible light efficiency in photocatalytic degradation of pollutants, Appl. Catal. B Environ. 180

(2016) 663–673.

[19] Q. Ma, X. Peng, M. Zhu, X. Wang, Y. Wang, H. Wang, Strategic modulation of electron migration in the TiO_2-Au-CdS: Z-scheme design for the enhancement in hydrogen evolution reaction, Electrochem. Commun. 95 (2018) 28–32.

[20] X. Wu, Y. Hu, Y. Wang, Y. Zhou, Z. Han, X. Jin, G. Chen, In-situ synthesis of Z-scheme Ag_2CO_3/Ag/AgNCO heterojunction photocatalyst with enhanced stability and photocatalytic activity, Appl. Surf. Sci. 464 (2019) 108–114.

[21] N. Lu, P. Wang, Y. Su, H. Yu, N. Liu, X. Quan, Construction of Z-Scheme g-C_3N_4/RGO/WO_3 with in situ photoreduced graphene oxide as electron mediator for efficient photocatalytic degradation of ciprofloxacin, Chemosphere 215 (2019) 444–453.

[22] Y. Sasaki, A. Iwase, H. Kato, A. Kudo, The effect of co-catalyst for Z-scheme photocatalysis systems with an Fe^{3+}/Fe^{2+} electron mediator on overall water splitting under visible light irradiation, J. Catal. 259 (2008) 133–137.

[23] F. Wang, W. Li, S. Gu, H. Li, X. Wu, C. Ren, X. Liu, Facile fabrication of direct Z-scheme MoS_2/Bi_2WO_6 heterojunction photocatalyst with superior photocatalytic performance under visible light irradiation, J. Photoch. Photobio. A 335 (2017) 140–148.

[24] W. Xue, D. Huang, G. Zeng, J. Wan, C. Zhang, R. Xu, M. Cheng, R. Deng, Nanoscale zero-valent iron coated with rhamnolipid as an effective stabilizer for immobilization of Cd and Pb in river sediments, J. Hazard. Mater. 341 (2018) 381–389.

[25] X. Lu, W. Che, X. Hu, Y. Wang, A. Zhang, F. Deng, S. Luo, D.D. Dionysiou, The facile fabrication of novel visible-light-driven Z-scheme $CuInS_2/Bi_2WO_6$ heterojunction with intimate interface contact by in situ hydrothermal growth strategy for extraordinary photocatalytic performance, Chem. Eng. J. 356 (2019) 819–829.

[26] G. Long, J. Ding, L. Xie, R. Sun, M. Chen, Y. Zhou, X. Huang, G. Han, Y. Li, W. Zhao, Fabrication of mediator-free g-C_3N_4/Bi_2WO_6 Z-scheme with enhanced photocatalytic reduction dechlorination performance of 2,4-DCP, Appl. Surf. Sci. 455 (2018) 1010–1018.

[27] Y. Su, G. Tan, T. Liu, L. Lv, Y. Wang, X. Zhang, Z. Yue, H. Ren, A. Xia, Photocatalytic properties of $Bi_2WO_6/BiPO_4$ Z-scheme photocatalysts induced by double internal electric fields, Appl. Surf. Sci. 457 (2018) 104–114.

[28] B. Li, C. Lai, G. Zeng, L. Qin, H. Yi, D. Huang, C. Zhou, X. Liu, M. Cheng, P. Xu, C. Zhang, F. Huang, S. Liu, Facile hydrothermal synthesis of Z-scheme $Bi_2Fe_4O_9/Bi_2WO_6$ heterojunction photocatalyst with enhanced visible light photocatalytic activity, ACS Appl. Mater. Inter. 10 (2018) 18824–18836.

[29] Z. Wang, T. Hu, K. Dai, J. Zhang, C. Liang, Construction of Z-scheme Ag_3PO_4/Bi_2WO_6 composite with excellent visible-light photodegradation activity for removal of organic contaminants, Chinese J. Catal. 38 (2017) 2021–2029.

[30] X.J. Wen, C.G. Niu, H. Guo, L. Zhang, C. Liang, G.M. Zeng, Photocatalytic degradation of levofloxacin by ternary Ag_2CO_3/CeO_2/AgBr photocatalyst under visible-light irradiation: Degradation pathways, mineralization ability, and an accelerated interfacial charge transfer process study, J. Catal. 358 (2018) 211–223.

[31] H. Zhao, G. Li, F. Tian, Q. Jia, Y. Liu, R. Chen, g-C_3N_4 surface-decorated $Bi_2O_2CO_3$ for improved photocatalytic performance: theoretical calculation and photodegradation of antibiotics in actual water matrix, Chem. Eng. J. 366 (2019) 468–479.

[32] D. Huang, Sha Chen, G. Zeng, X. Gong, C. Zhou, M. Cheng, W. Xue, X. Yan, J. Li, Artificial Z-scheme photocatalytic system: what have been done and where to go? Coordin. Chem. Rev. 385 (2019) 44–80.

[33] B. Chen, Y. Deng, H. Tong, J. Ma, Preparation, characterization, and enhanced visible-light photocatalytic activity of AgI/Bi_2WO_6 composite, Superlattice Microst. 69 (2014) 194–203.

[34] Y. Wang, W. Jiang, W. Luo, X. Chen, Y. Zhu, Ultrathin nanosheets g-C_3N_4@Bi_2WO_6 core-shell structure via low temperature reassembled strategy to promote photocatalytic activity, Appl. Catal. B Environ. 237 (2018) 633–640.

[35] Y. Deng, L. Tang, G. Zeng, J. Wang, Y. Zhou, J. Wang, J. Tang, Y. Liu, B. Peng, F. Chen, Facile fabrication of a direct Z-scheme Ag_2CrO_4/g-C_3N_4 photocatalyst with enhanced visible light photocatalytic activity, J. Mol. Catal. A-Chem. 421 (2016) 209–221.

[36] L. Yan, Y. Wang, H. Shen, Y. Zhang, J. Li, D. Wang, Photocatalytic activity of Bi_2WO_6/Bi_2S_3 heterojunctions: the facilitation of exposed facets of Bi_2WO_6 substrate, Appl. Surf. Sci. 393 (2017) 496–503.

[37] W.K. Jo, T.S. Natarajan, Influence of TiO_2 morphology on the photocatalytic efficiency of direct Z-scheme g-C_3N_4/TiO_2 photocatalysts for isoniazid degradation, Chem. Eng. J. 281 (2015) 549–565.

[38] X.J. Wen, C.G. Niu, R. Min, L. Zhang, G.M. Zeng, AgI nanoparticles-decorated CeO_2 microsheets photocatalyst for the degradation of organic dye and tetracycline under visible-light irradiation, J. Colloid. Interf. Sci. 497 (2017) 368–377.

[39] M. Xu, L. Han, S. Dong, Facile fabrication of highly efficient g-C_3N_4/Ag_2O heterostructured photocatalysts with enhanced visible-light photocatalytic activity, ACS Appl. Mater. Inter. 5 (2013) 12533–12540.

[40] P. Niu, L. Zhang, G. Liu, H.M. Cheng, Graphene-like carbon nitride nanosheets for improved photocatalytic activities, Adv. Funct. Mater. 22 (2012) 4763–4770.

[41] L. Huang, H. Xu, Y. Li, H. Li, X. Cheng, J. Xia, Y. Xu, G. Cai, Visible-light- induced WO_3/g-C_3N_4 composites with enhanced photocatalytic activity, Dalton T. 42 (2013) 8606–8616.

[42] T.Y. Wang, W. Quan, D. Jiang, L.L. Chen, D. Li, S.C. Meng, M. Chen, Synthesis of redox-mediator-free direct Z-scheme AgI/WO_3 nanocomposite photocatalysts for the degradation of tetracycline with enhanced photocatalytic activity, Chem. Eng. J. 300 (2016) 280–290.

[43] Y. Liu, P. Chen, Y. Chen, H. Lu, J. Wang, Z. Yang, Z. Lu, M. Li, L. Fang, In situ ion-exchange synthesis of SnS_2/g-C_3N_4 nanosheets heterojunction for enhancing photocatalytic activity, Rsc Adv. 6 (2016) 10802–10809.

[44] H. Wang, X. Yuan, H. Wang, X. Chen, Z. Wu, L. Jiang, W. Xiong, G. Zeng, Facile synthesis of Sb_2S_3/ultrathin g-C_3N_4 sheets heterostructures embedded with g-C_3N_4 quantum dots with enhanced NIR-light photocatalytic performance, Appl. Catal. B Environ. 193 (2016) 36–46.

[45] S. Adhikari, D.-H. Kim, Synthesis of Bi_2S_3/Bi_2WO_6 hierarchical microstructures for enhanced visible light driven photocatalytic degradation and photoelectrochemical sensing of ofloxacin, Chem. Eng. J. 354 (2018) 692–705.

[46] Y. Zhu, Y. Wang, Q. Ling, Y. Zhu, Enhancement of full-spectrum photocatalytic activity over $BiPO_4/Bi_2WO_6$ composites, Appl. Catal. B Environ. 200 (2017) 222–229.

[47] S. Meng, X. Ning, T. Zhang, S.F. Chen, X. Fu, What is the transfer mechanism of photogenerated carriers for the nanocomposite photocatalyst Ag_3PO_4/g-C_3N_4 band-band transfer or a direct Z-scheme? Phys. Chem. Chem. Phys. 17 (2015) 11577–11585.

[48] W. Ju, D. Fang, Z. Yan, X. Yi, Synthesis of Bi_2WO_6 nanoplate-built hierarchical nest-like structures with visible-light-induced photocatalytic activity, J. Phys. Chem. C 111 (2007) 12866–12871.

[49] C. Wen, W. Paul, J.A. Leenheer, B. Karl, Fluorescence excitation-emission matrix regional integration to quantify spectra for dissolved organic matter, Environ. Sci. Technol. 37 (2015) 5701–5710.

[50] X.J. Wen, C.G. Niu, L. Zhang, C. Liang, H. Guo, G.M. Zeng, Photocatalytic degradation of ciprofloxacin by a novel Z-scheme CeO_2-Ag/AgBr photocatalyst: influencing factors, possible degradation pathways, and mechanism insight, J. Catal. 358 (2018) 141–154.

[51] W. He, Y. Sun, G. Jiang, H. Huang, X. Zhang, F. Dong, Activation of amorphous Bi_2WO_6 with synchronous Bi metal and Bi_2O_3 coupling: photocatalysis mechanism and reaction pathway, Appl. Catal. B Environ. 232 (2018) 340–347.

[52] J.C.S. Fernandes, R. Picciochi, M.D.C. Belo, T.M.E. Silva, M.G.S. Ferreira, I.T.E. Fonseca, Capacitance and photoelectrochemical studies for the assessment of anodic oxide films on aluminium, Electrochim. Acta. 49 (2004) 4701–4707.

[53] C. Zeng, Y. Hu, H. Huang, BiOBr $_{0.7}$5$_{I0.2}$5/BiOI$_{O}$3 as a novel heterojunctional photocatalyst with superior visible-light-driven photocatalytic activity in removing diverse industrial pollutants, ACS Sustain Chem. Eng. 5 (2017) 3897–3905.

[54] B. Shao, Z. Liu, G. Zeng, Y. Liu, X. Yang, C. Zhou, M. Chen, Y. Liu, Y. Jiang, M. Yan, Immobilization of laccase on hollow mesoporous carbon nanospheres: noteworthy immobilization, excellent stability and efficacious for antibiotic contaminants removal, J. Hazard. Mater. 362 (2019) 318–326.

[55] Y. Yang, Z. Zeng, C. Zhang, D. Huang, G. Zeng, R. Xiao, C. Lai, C. Zhou, H. Guo, W. Xue, M. Cheng, W. Wang, J. Wang, Construction of iodine vacancy-rich BiOI/Ag@AgI Z-scheme heterojunction photocatalysts for visible-light-driven tetracycline degradation: transformation pathways and mechanism insight, Chem. Eng. J. 349 (2018) 808–821.

[56] Y. Tian, B. Chang, J. Lu, J. Fu, F. Xi, X. Dong, Hydrothermal synthesis of graphitic carbon nitride-Bi_2WO_6 heterojunctions with enhanced visible light photocatalytic activities, ACS Appl. Mater. Interfaces 5 (2013) 7079–7085.

[57] W. Chang, W. Xue, E. Liu, J. Fan, B. Zhao, Highly efficient H_2 production over $NiCo_2O_4$ decorated g-C_3N_4 byphotocatalytic water reduction, Chem. Eng. J. 362 (2019) 392–401.

[58] F. Chen, D. Li, B. Luo, M. Chen, W. Shi, Two-dimensional heterojunction photocatalysts constructed by graphite-like C_3N_4 and Bi_2WO_6 nanosheets: Enhanced photocatalytic activities for water purification, J. Alloy. Compd. 694 (2017) 193–200.

[59] D. Jiang, W. Ma, P. Xiao, L. Shao, D. Li, M. Chen, Enhanced photocatalytic activity of graphitic carbon nitride/carbon nanotube/Bi_2WO_6 ternary Z-scheme heterojunction with carbon nanotube as efficient electron mediator, J. Colloid. Interf. Sci. 512 (2018) 693–700.

[60] H. Liu, H. Zhou, H. Li, X. Liu, C. Ren, Y. Liu, W. Li, M. Zhang, Fabrication of Bi_2S_3@Bi_2WO_6/WO_3 ternary photocatalyst with enhanced photocatalytic performance: synergistic effect of Z-scheme/traditional heterojunction and oxygen vacancy, J. Taiwan Inst. Chem. E. 95 (2019) 94–102.

[61] C. Li, G. Chen, J. Sun, J. Rao, Z. Han, Y. Hu, W. Xing, C. Zhang, Doping effect of phosphate in Bi_2WO_6 and universal improved photocatalytic activity for removing various pollutants in water, Appl. Catal. B Environ. 188 (2016) 39–47.

[62] A. Yuan, H. Lei, F. Xi, J. Liu, L. Qin, Z. Chen, X. Dong, Graphene quantum dots decorated graphitic carbon nitride nanorods for photocatalytic removal of antibiotics, J. Colloid. Interf. Sci. 548 (2019) 56–65.

[63] M.A. Rauf, M.A. Meetani, A. Khaleel, A. Ahmed, Photocatalytic degradation of Methylene Blue using a mixed catalyst and product analysis by LC/MS, Chem. Eng. J. 157 (2010) 373–378.